Laboratory study of the cross-shore flow structure in the surf and swash zones

In Mei Sou[1] and Harry Yeh[2]

Received 5 October 2010; revised 16 November 2010; accepted 16 December 2010; published 2 March 2011.

[1] The flow structure of oscillatory broken waves within surf and swash zones was investigated using particle image velocimetry (PIV) in the laboratory. With the resolved spatial distribution of the velocity field, vorticity was computed directly. The results show that flow separation at the bed occurs during the interaction between the uprush bore front and the downwash flow. The separation point advances in the onshore direction with the bore front until the bore reaches the lowest point of the moving shoreline. The bore front continues to climb up onshore and collapses at the highest point of the moving shoreline. In the swash zone, flow attachment to the bed occurs during the transition from the uprush to downwash process. An internal flow circulation is generated at the flow reversal phase as the flow near the bed responds to the gravitational force earlier than the flow in the upper water column, where the uprush momentum is sustained later in phase. The magnitude of the downwash velocity in the swash zone is greater than that of the uprush process. The swash zone flow observed in the experiments should be erosive in the lower part of the swash and accretive in the upper part where flow attachment occurs.

Citation: Sou, I. M., and H. Yeh (2011), Laboratory study of the cross-shore flow structure in the surf and swash zones, *J. Geophys. Res.*, *116*, C03002, doi:10.1029/2010JC006700.

1. Introduction

[2] Flows in the surf and swash zones have received increasing attention in recent years. Most researchers have mainly focused on the shoreline motions [*Yeh et al.*, 1989; *Holland et al.*, 1995; *Raubenheimer and Guza*, 1996; *Hughes*, 2004]. Less attention has been focused on the flow structure. Recently, successful efforts have been made to measure velocity in the surf and swash zones in the field [*Raubenheimer*, 2002; *Raubenheimer et al.*, 2004; *Butt et al.*, 2004] but with limited vertical resolution.

[3] The traditional definition of the swash is a zone where wave runup covers and uncovers the beach face periodically. It is difficult to make measurements in such a thin and aerated flow even in the well-controlled laboratory environment. Most laboratory studies using laser Doppler velocimetry (LDV) extends the definition of swash zone farther offshore into the inner surf zone due to the difficulty in accessing the thin water depth [*Hwung et al.*, 1998; *Petti and Longo*, 2001]: Note that measurement regions within the extended swash zone may not become periodically dry. In this study, the swash zone is defined as the region within the moving shoreline.

[4] There are many laboratory studies on breaking waves in the surf and swash zone using LDV. *Stive* [1980] and *Nadaoka and Kondoh* [1982] are among the pioneers. *Stive* [1980] investigated the internal flow velocity field of a quasi-steady spilling breaker in the surf zone. *Nadaoka and Kondoh* [1982] studied the velocity flow field inside the surf zone to clarify the dependence of sand movements upon the bottom velocity. *Ting and Kirby* [1994, 1995, 1996] investigated the differences in the turbulence characteristics between plunging and spilling breakers. They found that turbulent kinetic energy (TKE) is transported seaward under a spilling breaker and landward under a plunging breaker. *Feng and Stansby* [2005] investigated the flow structure of a spilling breaker in the surf zone. Using the wave phase speed, c, to connect space and time as $\partial/\partial t = -c\partial/\partial x$, *Feng and Stansby* [2005] transformed the LDV temporal velocity measurements to spatial velocity fields. They found that a convergent stagnation point is located on the bed in the initial breaker zone and the inner surf zone, but a divergent stagnation point is found in a small region after the initial breaker. For the swash zone, *Hwung et al.* [1998] performed a resolved phase-dependent LDV measurement of the vertical structure of swash flows. They observed that a vertically growing turbulent bottom boundary layer in the swash zone formed on a smooth bed. *Petti and Longo* [2001] performed a turbulence analysis of swash flows on a concrete beach using LDV. They found that the turbulence level is much higher during uprush than downwash phases in plunging and collapsing breakers.

[1]Department of Civil and Environmental Engineering, University of Hawai'i at Mānoa, Honolulu, Hawaii, USA.
[2]School of Civil and Construction Engineering, Oregon State University, Corvallis, Oregon, USA.

0148-0227/11/2010JC006700

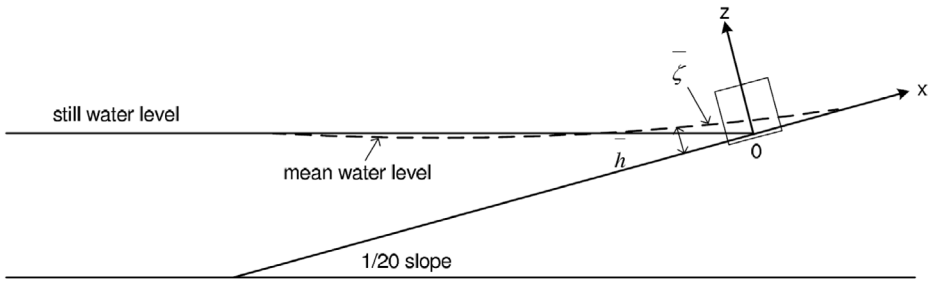

Figure 1. Experiment coordinate system ($x - z$ plane).

[5] Many researchers have taken advantage of the ability of the particle image velocimetry (PIV) technique to obtain two-dimensional flow fields in wave environments. *Dabiri and Gharib* [1997] studied the vorticity generation within a spilling water wave using the PIV technique. *Chang and Liu* [1996, 1998, 1999] examined the flow field and turbulence structure of quasi-periodic breaking waves. They measured the velocity near the tip of an overturning jet and found that the maximum velocity is 1.68 times of the phase speed. *Cox and Anderson* [2001] observed large vortices in the horizontal plane in the outer surf zone, which is indicative of the existence of obliquely descending eddies in the outer surf zone. *Melville et al.* [2002] studied the coherent structures of a breaking wave in a channel flow. *Cowen et al.* [2003] used a PIV technique to quantify the evolution of TKE and dissipation of plunging and spilling forced swash zones in the laboratory. The temporal TKE decay was found to behave similarly to grid turbulence decay during the latter stage of uprush and the early stage of the downwash. *Sou et al.* [2010] examined the evolution of the turbulence structure from the outer surf zone to the swash zone using the same PIV velocity fields presented in this paper. They concluded that the temporal evolution of the turbulence can be divided into three intervals over a wave cycle: (1) the wave-breaking-generated turbulence and the shear-layer-generated turbulence at the bore front phases at which the large-scale turbulence is generated; (2) a decay stage, analogous to grid turbulence decay during the latter part of uprush and the early part of the downwash phases; and (3) the phases dominated by the bed-generated turbulence, yielding the −1 spectral law during the latter part of the downwash phases.

[6] Different from the earlier studies by *Cowen et al.* [2003] and *Sou et al.* [2010], this paper investigates the fundamental characteristics of the flow structure in the vertical cross-shore plane as the wave evolves from the outer surf zone to the swash zone. We describe the experiments and data analysis methods in section 2. The results are presented in section 3. The phase-averaged velocity and vorticity fields of the flows are examined in sections 3.1 and 3.2. More detailed discussion is focused on the interaction between the bore front and downwash (in section 3.3), the reversal flow field (in section 3.4) and the surf and swash velocity characteristics (in section 3.5). Conclusions are presented in section 4.

2. Experimental Setup

[7] The experiments were performed in a wave tank (32 m long, 0.6 m wide and 0.9 m deep) with painted steel bottom and glass sidewalls. A hydraulically driven piston-type wave maker is located at one end of the tank. An integrated system for the wave maker motions and the measurements was developed to trigger the PIV Yag laser and the camera at the precise timings. A 1:20 sloping glass beach supported by a stainless steel frame is placed at the other end of the tank: note that the toe of the beach is located 19 m from the wave maker. We define our coordinate system such that x is positive onshore along the beach surface. The location $x = 0$ is placed at the intersection of the still water level with the beach. The z direction is defined normal to the beach face and positive upward. The y axis is set by the right-hand rule with $y = 0$ at the lateral midpoint of the tank as shown in Figures 1 and 2.

[8] We set the offshore water depth at 26.0 cm and generate a monochromatic wave with period $T = 2.0$ seconds. The incident wave height was $H = 2.46$ cm, which was measured 9 m from the wave maker using a capacitance-type wave gage. This wave condition generated a plunging breaker characterized by the surf similarity parameter $\xi = \tan\gamma/\sqrt{H/\lambda} = 0.56$ [*Battjes*, 1974], where γ (=2.86°) is the angle of beach slope from the horizontal and λ is the wave length, determined from the dispersion relation using the offshore water depth and wave period.

[9] Due to the different local water depths, the PIV image size varies from the offshore location to the onshore location with decreasing size in the field of view. Three measurement areas are within the surf zone while one measurement area is within the swash zone. We refer to the four measurement areas as $\mathcal{A}_1$ (centered at $x = -55$ cm), $\mathcal{A}_2$ (centered at $x = -30$ cm), $\mathcal{A}_3$ (centered at $x = 0$ cm, the still water line), and $\mathcal{A}_4$ (centered at $x = 17.5$ cm). The variations of phase-averaged water depths $\langle h \rangle$ were: 2.2 cm $\leq \langle h \rangle \leq$ 4.3 cm in $\mathcal{A}_1$; 1.3 cm $\leq \langle h \rangle \leq$ 2.9 cm in $\mathcal{A}_2$; 0.5 cm $\leq \langle h \rangle \leq$ 1.6 cm in $\mathcal{A}_3$; and 0 cm $\leq \langle h \rangle \leq$ 0.8 cm in $\mathcal{A}_4$. The wave starts breaking roughly at −80 cm. It is emphasized that the water depths in the swash zone $\mathcal{A}_4$ were extremely shallow and the PIV measurements were taken at 30 cm from the sidewall, i.e., at the center of the tank. The detailed PIV laser information and PIV image processing for instantaneous velocity fields as well as the uncertainty analysis are given by *Sou et al.* [2010].

[10] Detailed investigation of the velocity field near the free surface is challenging due to the local uncertainty in free surface position at the bore front phase as the free surface is not itself discernible due to the use of the optical filter. Hence, we will not attempt to look into the instantaneous free surface velocities, but will focus on the bulk and near bed flow structure. Furthermore, we choose to examine the phase-averaged quantities of the flow because we would

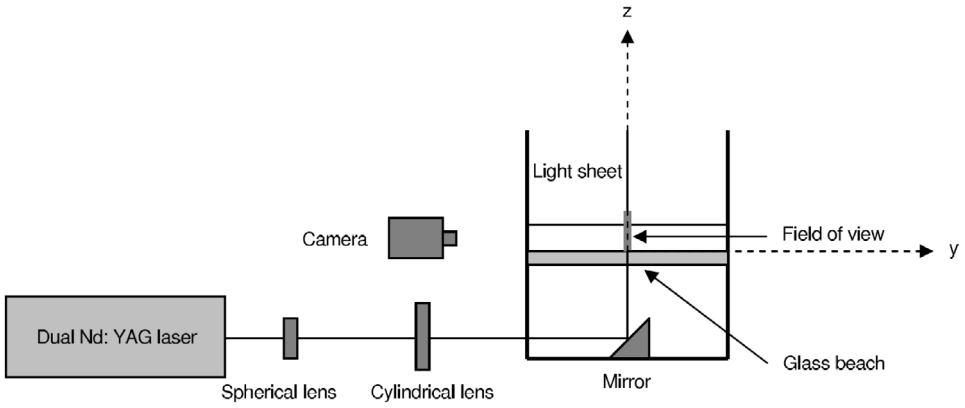

Figure 2. Schematic sketch of the experimental setup viewed from the end of the wave tank ($y - z$ plane).

like to gain the insight of the mechanisms of material transports (e.g., sediment transport in the flow) in the surf and swash zone over a long period of time. In addition, a single wave cannot reveal detailed information on the flow due to the limited range of our PIV data as the measurements at the four locations ($\mathcal{A}_1 - \mathcal{A}_4$) were made separately by repeating the experiments. Our phase averaging requires a high repeatability of wave to wave motion. The repeatability test was performed using the free surface profiles at each cross-shore location. The average ratio of the root-mean-square free surface deviation to the phase-averaged water depth among all locations is 0.05. The test shows that the wave condition is highly repeatable (for more complete explanation for the repeatability, see *Sou et al.* [2010]).

[11] The phase average of a periodic quantity, with replication period T, and total temporal length $T' = NT$, where N is the number of periods in the record (i.e., 200 in the present case), is defined as

$$\langle \Theta(\tau) \rangle = \frac{1}{N} \sum_{n=0}^{N-1} \Theta(\tau + nT), \text{where } \tau \text{ lies in the interval } \{0, T\}. \tag{1}$$

Given $T = 2.0$ s and the PIV data rate of 15 Hz, 30 wave phases were resolved within each wave period.

[12] Denoting the phase-averaged velocity vector $\langle \vec{u} \rangle = (\langle u \rangle, \langle v \rangle, \langle w \rangle)$ in (x, y, z), the spanwise phase-averaged vorticity component

$$\langle \omega_y \rangle = \frac{\partial \langle u \rangle}{\partial z} - \frac{\partial \langle w \rangle}{\partial x} \tag{2}$$

was computed from the entire phase-averaged velocity fields using the central difference method as

$$\langle \omega_y(i,j) \rangle = \frac{\langle u(i,j+1) \rangle - \langle u(i,j-1) \rangle}{2\Delta z} - \frac{\langle w(i+1,j) \rangle - \langle w(i-1,j) \rangle}{2\Delta x}, \tag{3}$$

where (i, j) represents the spatial grid point in (x, z). Positive vorticity is defined based on the right-hand rule. Base on the coordinate system presented in Figure 1, positive vorticity is clockwise (CW) and negative is counterclockwise (CCW). As our instantaneous free surface profiles were obtained by curve fitting [*Sou et al.*, 2010], detailed free surface information cannot be obtained from the data. We decided not to treat the vorticity near the free surface in a special way. Such a special treatment has been made by *Dabiri and Gharib* [1997] who assumed a no-shear boundary condition at the free surface to calculate the vorticity in order to minimize the artificial shear layer; they replaced all velocity vectors above the last valid velocity vector near the free surface by that same velocity vector for each column within the velocity field before vorticity was calculated.

3. Results

3.1. Phase-Averaged Velocity Field in the Surf and Swash Zones

[13] A distinct advantage of spatiotemporal data sets, yielded by PIV, is that one does not need to rely on the use of a mean velocity to connect space and time; an assumption often made in interpreting purely temporal data sets, such as those collected by LDV. The representative phase-averaged velocity fields during the uprush, reversal, and downwash phases at the four cross-shore locations in the surf and swash zones are shown in Figure 3. Our camera was synchronized to capture the PIV images at the same global time at each location with respect to a reference phase that is the wave paddle position in our case. The sequence of images shown in Figure 3 can be viewed as snap shots of the flow field covering the outer surf zone to the swash zone for six different timings. The local bore front arrival is set at the phase $t/T = 0$, hence globally the local phase differs at different cross-shore measurement locations at the same instant in time. Note that the velocity vectors shown in Figure 3 are scaled in order to present the flow patterns more clearly, i.e., the velocity magnitude scale is different for Figures 3a–3x, and also the spatial scales of each measurement location are different.

[14] When the bore front overtakes the downwash, a shear layer is formed. While a very strong shear layer is evident at the location of the initial shoreline $\mathcal{A}_3$ (see Figure 3k at the phase $t/T = 0$), the shear layers at the offshore locations($\mathcal{A}_1$ and $\mathcal{A}_2$, see Figures 3a and 3f, respectively) are relatively weak. Also note that a sign of flow separation is observed near the bed at $x = -28$ cm in Figure 3f at the phase 30 $t/T = 1$

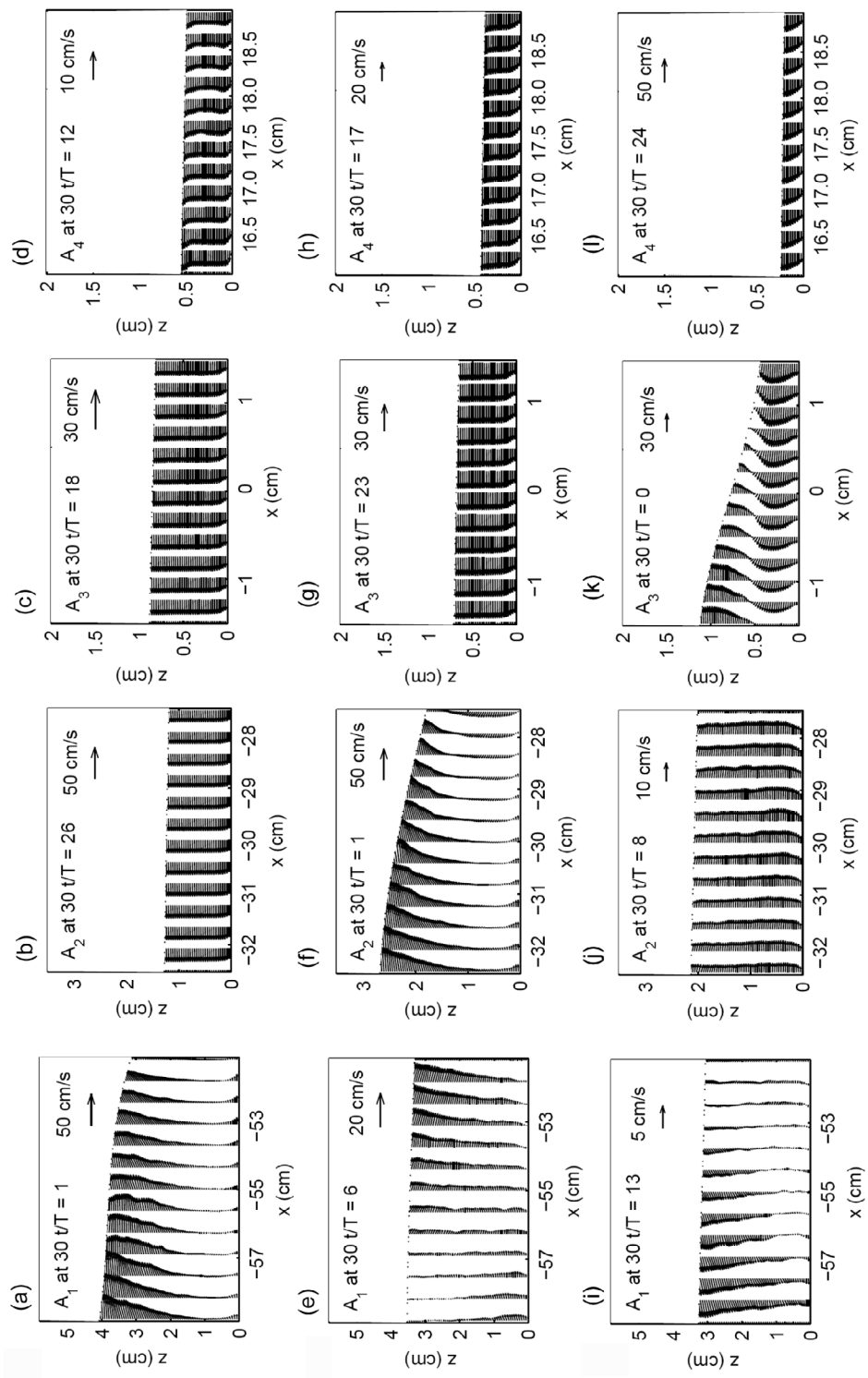

Figure 3. Synchronized phase-averaged velocity at the measurement locations $\mathcal{A}_1$, $\mathcal{A}_2$, $\mathcal{A}_3$, and $\mathcal{A}_4$ in the surf and swash zones; every tenth vector in the horizontal is shown and the velocity vectors are dynamically scaled for improved visibility. Phases at $\mathcal{A}_1$, $\mathcal{A}_2$, $\mathcal{A}_3$, and $\mathcal{A}_4$ are (a–d) 30 t/T = 1, 26, 18, 12; (e–h) 30 t/T = 6, 1, 23, 17; (i–l) 30 t/T = 13, 8, 0, 24; (m–p) 30 t/T = 17, 12, 4, 28; (q–t) 30 t/T = 23, 18, 10, 4; and (u–x) 30 t/T = 28, 23, 15, 9. Note that the axis scales are different in order to show detailed velocity profiles.

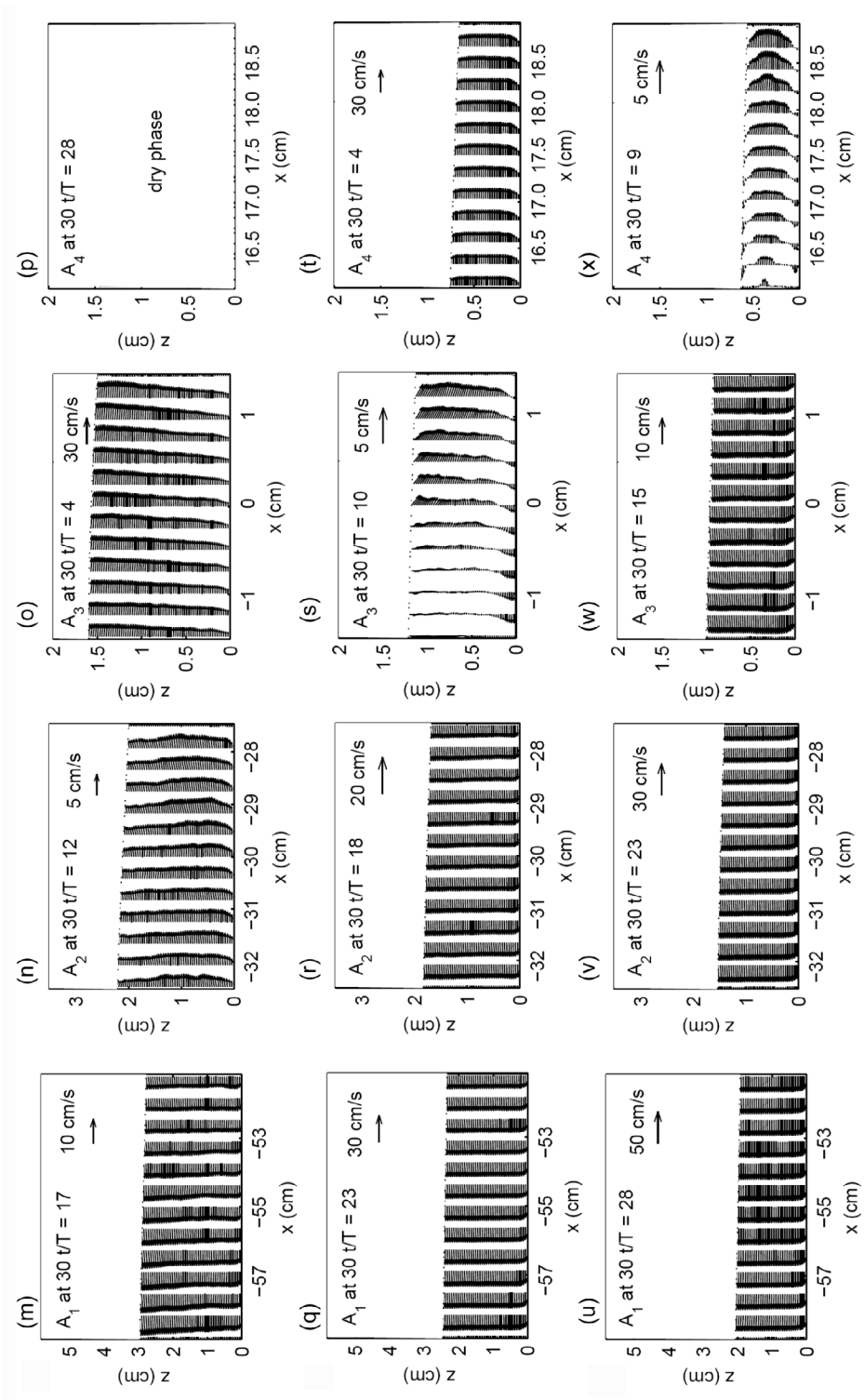

Figure 3. (continued)

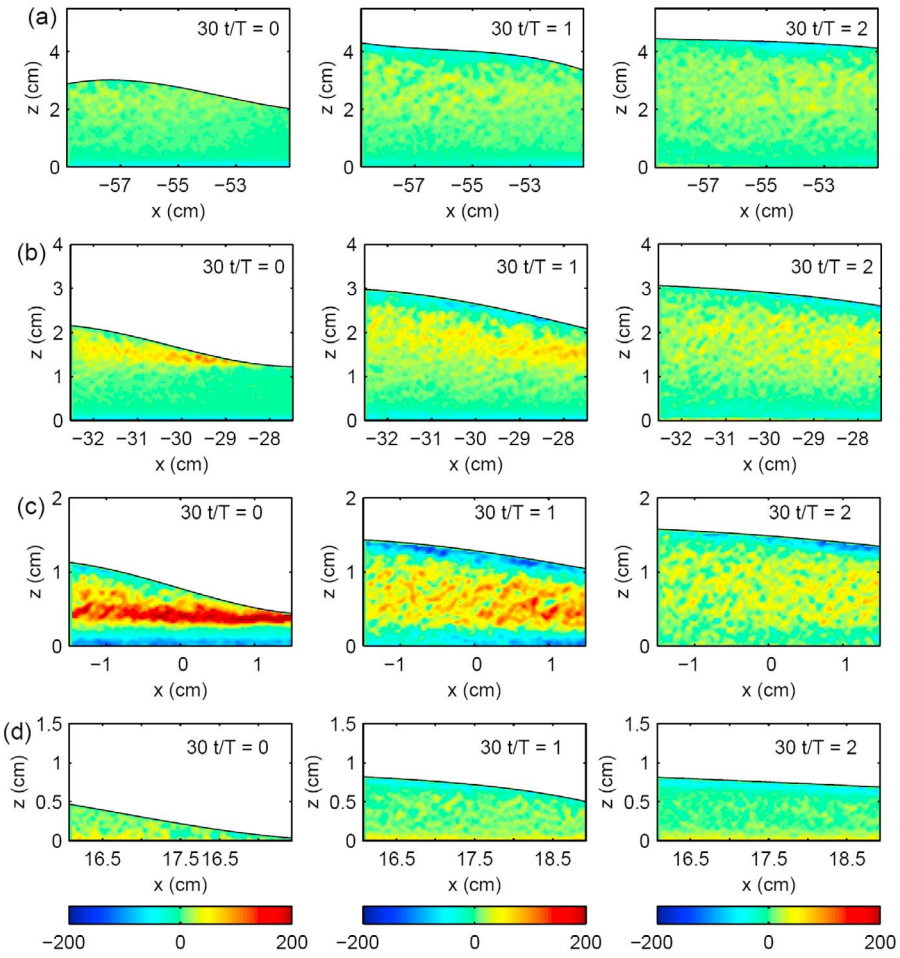

Figure 4. Phase-averaged vorticity (s^{-1}) at the initial uprush phases at the measurement area: (a) $\mathcal{A}_1$, (b) $\mathcal{A}_2$, (c) $\mathcal{A}_3$, and (d) $\mathcal{A}_4$ (positive is CW; negative is CCW).

as the reverse flow near the boundary shows the separation flow. This will be further discussed in section 3.3. At the swash location, $\mathcal{A}_4$, no such shear layer develops because the water advances on the dry surface without counter flow there.

[15] At the location $\mathcal{A}_2$, the momentum of the bore front spreads down quickly to the bed, returning the flow to unidirectional (Figures 3b, 3f, and 3j). During the downwash phases, the flow accelerates in the offshore direction throughout until the next bore front washes up the measurement area (see locations $\mathcal{A}_1$ and $\mathcal{A}_2$ in Figures 3m, 3q, and 3u and 3n, 3r, and 3v, respectively).

[16] A careful observation of the time sequence of the flow patterns at $\mathcal{A}_1$ shows that the flow reversal due to the approaching wave trough commences earlier near the surface and the bed than the interior flow: see Figures 3e and 3i. A similar behavior can be seen at $\mathcal{A}_3$ (Figure 3s) and at the swash $\mathcal{A}_4$ (Figure 3x). This behavior near the bed can be explained by the sensitivity of the boundary layers to local pressure gradients (will be discussed in section 3.4).

3.2. Phase-Averaged Vorticity Field in the Surf and Swash Zones

[17] The evolution of the vorticity in the surf and swash zones is examined. Figure 4 shows the vorticity fields during the uprush phases; those during the downwash phases are shown in Figure 5. The vorticity fields at the bore front phases are shown in Figure 4 (left) for the measurement locations $\mathcal{A}_1$, $\mathcal{A}_2$, $\mathcal{A}_3$, and $\mathcal{A}_4$.

[18] In the surf zone (Figures 4a–4c), the CCW (negative) vorticity that is present near the bed during the downwash phase still remains apparent at the bore front phases. Due to the CW (positive) vorticity associated with the surface roller together with the near-bed-generated CW vorticity in the uprush phase, the CCW vorticity near the bed decreases in strength. The CW vorticity at the bed is diffused up the water column as uprush phase advances. The strength of vorticity in the water column decays as phase advances during the later part of the uprush phase and the early part of the downwash phase (see Figure 5).

[19] All of the locations, except $\mathcal{A}_4$, exhibit the similar pattern of vorticity field at the initial uprush phase (Figure 4): positive (CW) inside of the fluid domain and negative (CCW) along the boundaries, both along the bed and the free surface. It is especially so at $\mathcal{A}_3$ (Figure 4c). The formation of the positive (CW) vortical layer represents shear resulting from the collision of incoming uprush flow and receding downwash flow; strong CW vorticity was present in the region in bright red and yellow in Figures 4b and 4c.

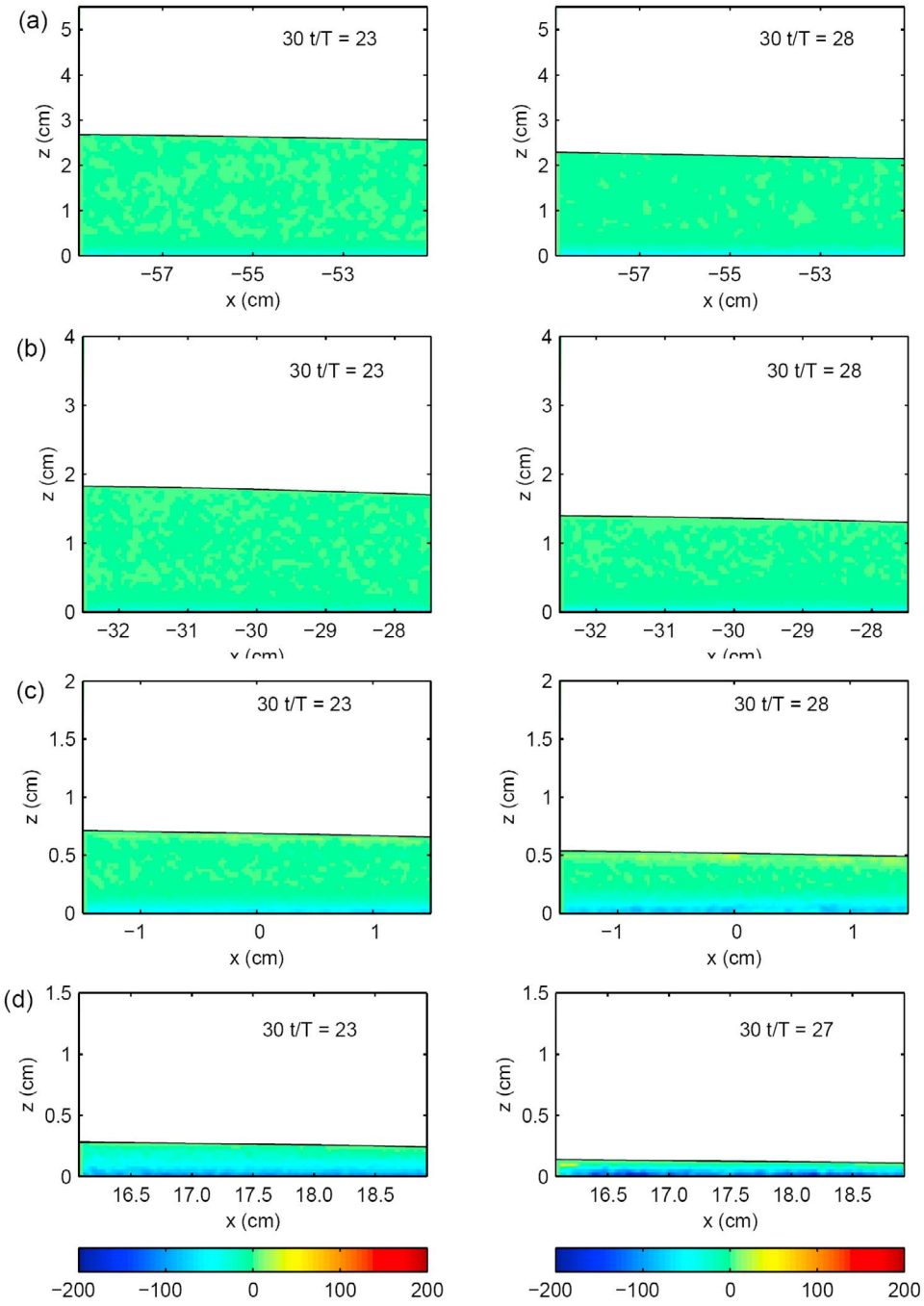

Figure 5. Phase-averaged vorticity (s^{-1}) at downwash phases at the measurement area: (a) $\mathcal{A}_1$, (b) $\mathcal{A}_2$, (c) $\mathcal{A}_3$, and (d) $\mathcal{A}_4$ (positive is CW; negative is CCW).

Mechanism of vorticity creation in the bore and the consequent shear layer formation were discussed by *Yeh* [1991].

[20] On the other hand, no such distinct layer of strong CW vortical flow is present at $\mathcal{A}_1$. The location $\mathcal{A}_1$ is right after the wave breaking point, hence, it appears that the wave breaking itself could not create strong fluid rotation (i.e., vorticity). Instead of the strong vorticity layer similar to $\mathcal{A}_2$ and $\mathcal{A}_3$, weak CW vorticity is observed approximately in the upper half water column of the flow at $\mathcal{A}_1$ (Figure 4a).

[21] To justify the presence of the foregoing negative vorticity along the water surface, we consider the flow circulation by taking a closed contour in the flow domain bounded by the free surface and the bed. We choose contour paths across the domain (connecting the free surface and the bed) so that the tangential component of velocity along the path vanishes at a given instant, i.e., the path is kept normal to the velocity vector; hence not necessarily a vertical straight line. Given the velocity along the bed is zero because of no-slip condition, the flow circulation along the closed contour must be equal to the line integration of the velocity along the upper boundary of the domain adjacent to the real free surface. This flow circulation must be equal to

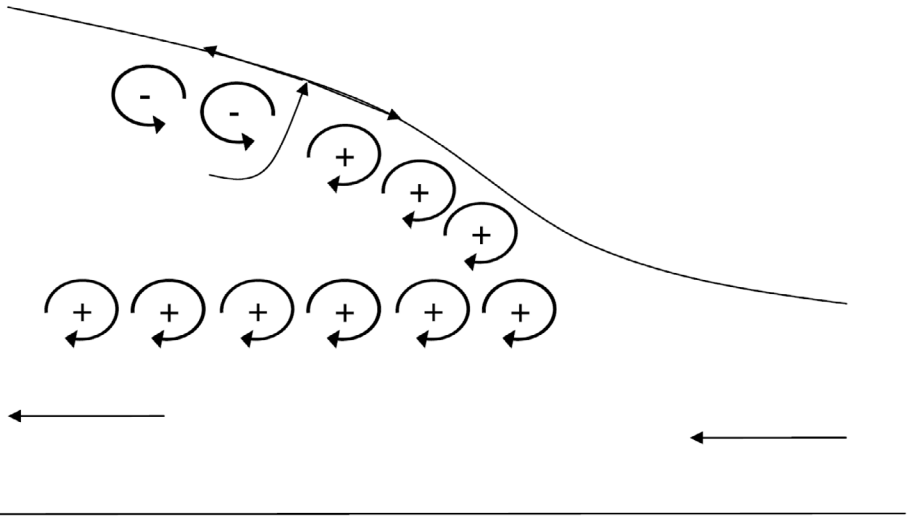

Figure 6. Schematic sketch of the physical mechanism for the CCW vorticity near the surface. The sketch is in the frame moving with the bore front.

the integrated vorticity within the domain enclosed by the circulation contour, it is the consequence of Stokes theorem. It must be valid for the unsteady flow. Note that as discussed earlier, our PIV cannot measure the actual water surface velocity, but the velocities adjacent to the water surface.

[22] The total quantities of the flow circulation during the three uprush phases ($30t/T = 0$, 1 and 2) are calculated to be 0.0374 m^2/s, 0.0345 m^2/s, 0.0194 m^2/s, and 0.0155 m^2/s for the locations $\mathcal{A}_1$, $\mathcal{A}_2$, $\mathcal{A}_3$, and $\mathcal{A}_4$, respectively. The quantities of the integrated vorticity within the domain during the uprush phases ($30t/T$ = 0, 1 and 2) are 0.0249 m^2/s, 0.0323 m^2/s, 0.0201 m^2/s, and 0.00840 m^2/s for the locations $\mathcal{A}_1$, $\mathcal{A}_2$, $\mathcal{A}_3$, and $\mathcal{A}_4$, respectively. As expected, the circulation is roughly balanced with the integrated vorticity; particularly the excellent agreement for the locations $\mathcal{A}_2$ (0.0345 m^2/s vs 0.0323 m^2/s) and $\mathcal{A}_3$ (0.0194 m^2/s vs 0.0201 m^2/s) are remarkable. Highest discrepancy is found for the location $\mathcal{A}_4$ (0.0155 m^2/s vs 0.00840 m^2/s). Because Stokes theorem must hold for any differentiable vector field in a simply connected domain, the discrepancy is related to imprecision in velocity measurements and vorticity computations in such a small domain (the flow depth less than 1 cm), especially near the free surface and the boundary layer along the bed. The discrepancy in the location $\mathcal{A}_1$ has to be associated with the measurements, also. The vorticity near the free surface could be underestimated due to the presence of entrained air bubbles right after the plunging breaker. Regardless, the excellent agreement in the locations $\mathcal{A}_2$ and $\mathcal{A}_3$ indicates that the strong appearance of negative (CCW) vorticity near the surface is consistent with the excessively large positive (CW) vorticity resulted from the collision of incoming uprush flow and receding downwash flow.

[23] The underlying physical mechanism for this CCW vorticity near the surface could be explained as follows. In the frame moving with the bore propagation, the water on the front face must move faster than the propagation speed, hence the formation of surface roller. On the other hand, the water behind the front face must move slower than the propagation speed, i.e., moves backward in the moving coordinate frame. This creates the flow divergence on the surface somewhere on the front face of the bore as depicted in Figure 6. This necessarily results in the CCW vorticity near the surface behind the front face, note that vorticity is Galilean invariant.

[24] Due to the absence of the downwash flow at $t/T = 0$ in the swash zone $\mathcal{A}_4$ as the bed is dry at the last downwash phase (Figure 4d), the flow is unidirectional at $t/T = 0$ in the swash zone. Therefore, the flow is dominated by CW vorticity generated at the bed in the swash zone. A layer of CCW vorticity near the free surface is apparent at $30\ t/T = 1$ at the location $\mathcal{A}_4$ (Figure 4d). It is believed that this CCW vorticity layer is advected from the location $\mathcal{A}_3$: as discussed, the negative (CCW) vorticity is induced near the surface due to the collision of the uprush and downwash flows. The CW vorticity generated from the uprush flow at the boundary is not able to diffuse up to the surface due to the short uprush duration (relative to the flow depth) in the swash zone. During the downwash phase, on the other hand, the CCW vorticity generated at the bed diffuses over the entire water column at the end of the downwash phase (Figure 5d). The vorticity is confined by the water surface during the latter part of the downwash phase in the swash zone.

[25] The spatial variation of the phase-averaged vorticity indicates that the CCW vorticity strength during the downwash phase is dependent on the duration of the downwash phase. The flow reverses direction from uprush to downwash at the phase $30\ t/T$ = 13, 12, 10, and 9 for the locations $\mathcal{A}_1$, $\mathcal{A}_2$, $\mathcal{A}_3$, and $\mathcal{A}_4$, respectively. The longer the duration of the downwash phase, the stronger the CCW vorticity. The local maximum values of the CCW vorticity during downwash are $-30\ s^{-1}$, $-50\ s^{-1}$, $-100\ s^{-1}$, and $-150\ s^{-1}$ for the four measurement locations $\mathcal{A}_1$, $\mathcal{A}_2$, $\mathcal{A}_3$, and $\mathcal{A}_4$, respectively. The CW vorticity strength at the bore front is dependent on the shear layer strength; the global maximum of CW vorticity $350\ s^{-1}$ occurs at the strong shear layer in the inner surf zone, $\mathcal{A}_3$ at $30\ t/T = 0$ in Figure 4c. The local maximum of CW vorticity at $\mathcal{A}_1$ and $\mathcal{A}_2$ are $60\ s^{-1}$ and $215\ s^{-1}$, respectively. These results indicate that the initial

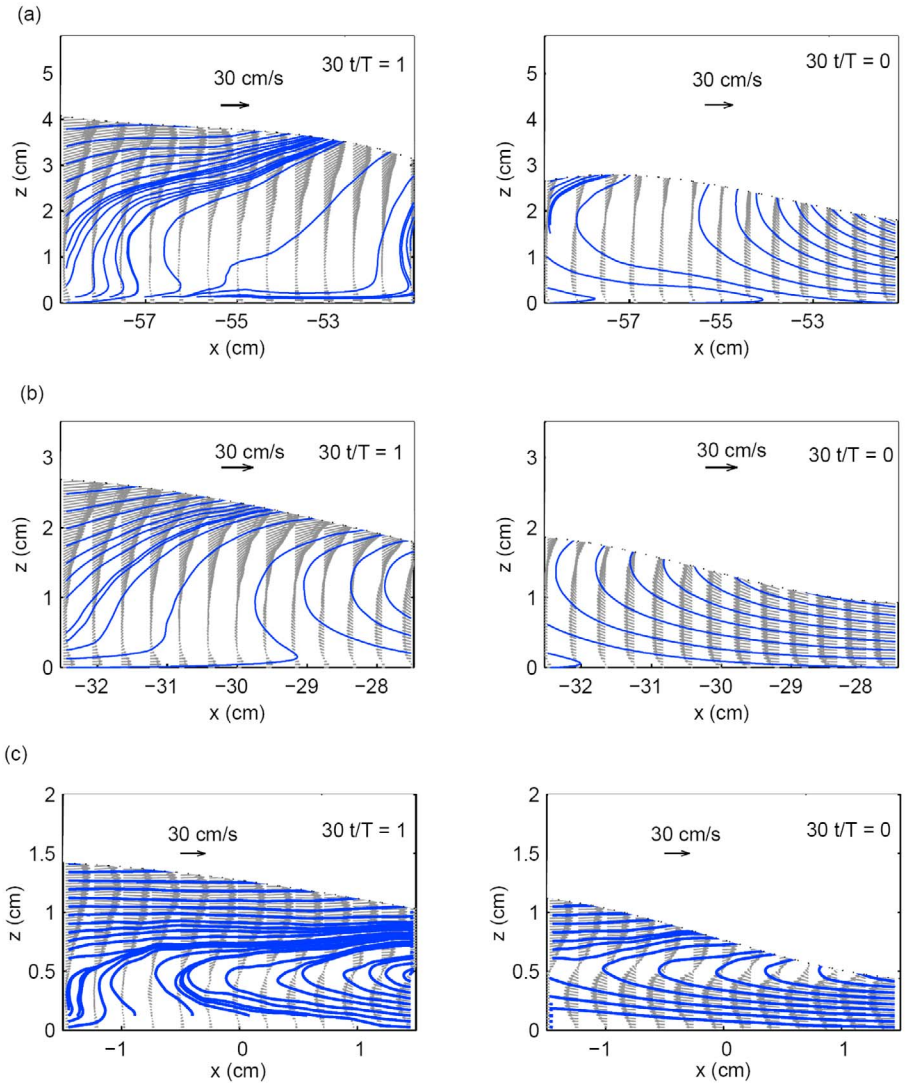

Figure 7. Phase-averaged velocity vector field and streamlines at the bore front phases (30 t/T = 0 and 1): (a) $\mathcal{A}_1$, (b) $\mathcal{A}_2$, and (c) $\mathcal{A}_3$.

shoreline location, $\mathcal{A}_3$, is influenced the most by the vortical flows.

3.3. The Interaction Between the Bore Front and the Downwash Flow in the Surf Zone

[26] In order to examine closely the flow field near the bed, we use the streamlines of the phase-averaged velocity field. The streamlines superimposed on the velocity field at the bore front phases (30 t/T = 0 and 1) at the measurement locations $\mathcal{A}_1$, $\mathcal{A}_2$, and $\mathcal{A}_3$ are shown in Figure 7. Figures 7a–7c are arranged so that the broader flow pattern can be examined conveniently by allowing the coordinate translation for a very short period, t/T = 1/30 s. Note that no data at location $\mathcal{A}_4$ is presented because the downwash flow is engulfed by the incident bore far offshore and no interaction is observed at location $\mathcal{A}_4$. Comparing the velocity contours at the locations $\mathcal{A}_1$, $\mathcal{A}_2$, and $\mathcal{A}_3$, the velocity gradient $\partial\langle u\rangle/\partial z$ at the shear layer is much stronger at the initial phase t/T = 0 at the inner surf zone location $\mathcal{A}_3$ (Figure 7c) than the other two locations $\mathcal{A}_1$ and $\mathcal{A}_2$ (Figures 7a and 7b). At the location $\mathcal{A}_3$, the velocity field indicates that a steep velocity gradient occurs between z = 0.3 cm to 0.6 cm at t/T = 0 as shown in Figure 7c. The streamlines indicate that the ratio of the uprush depth to downwash depth plays a role in determining the strength of the shear layer generated at the bore front phase. For each location, the maximum uprush depth and minimum downwash depth are defined as the maximum depth of the incoming bore and the minimum depth of the downwash flow. The ratio of the maximum $\langle h\rangle$ to the minimum $\langle h\rangle$ are 1.95, 2.23, and 3.20 for $\mathcal{A}_1$, $\mathcal{A}_2$, and $\mathcal{A}_3$, respectively. When the depth ratio is high ($\mathcal{A}_3$), the streamline above the trough level is relatively parallel to the bed (30 t/T = 1 at $\mathcal{A}_3$ in Figure 7c), which indicates that the momentum above the trough level dominates the initiation of the uprush. The same is true for the downwash flow: the streamlines are parallel to the bed (see Figure 7c at 30 t/T = 0). As a result, the streamlines change their direction with very tight turns. Our results indicate that the

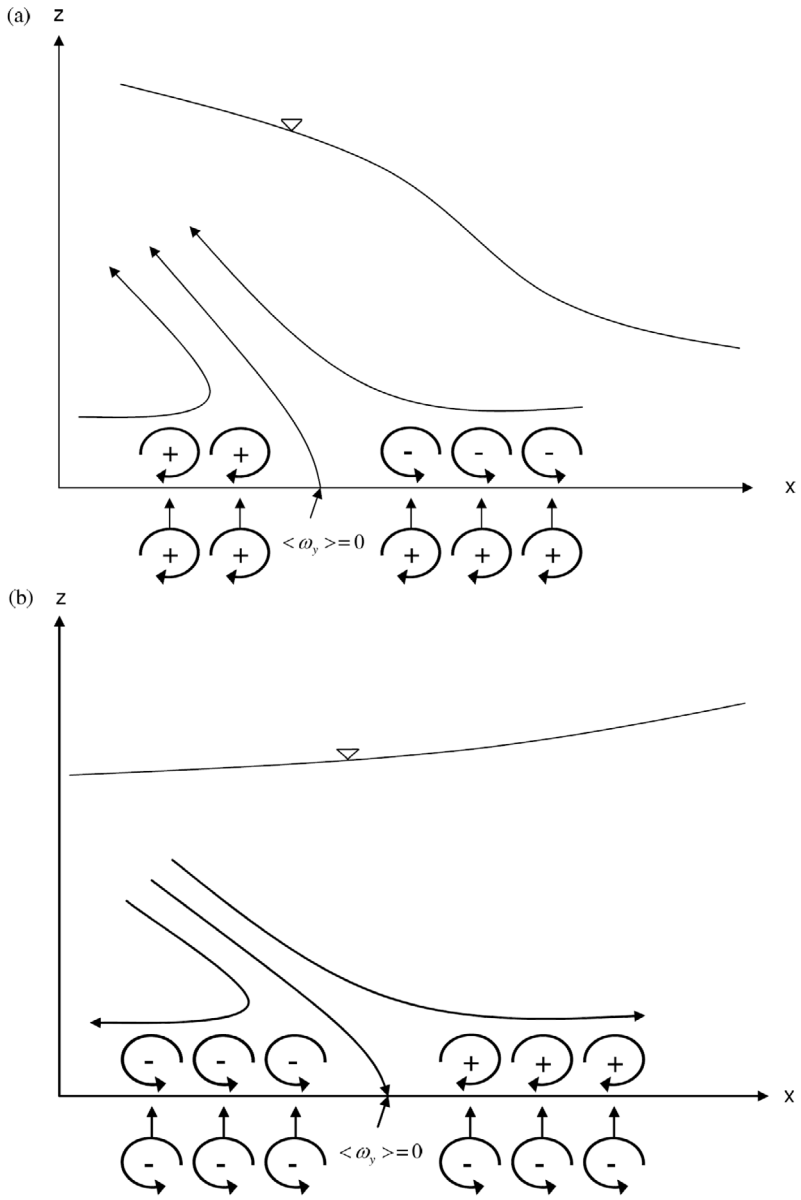

Figure 8. Schematic sketch of vorticity and vorticity flux out of the bed during (a) flow separation and (b) flow attachment.

higher the depth ratio, the stronger the shear layer, and also the flow patterns are different depending on the locations after wave breaking.

[27] The streamline pattern also implies that flow separation occurs at the bed under the bore front. The separation point in a two-dimensional flow is defined as the point on the bed where vorticity $\langle\omega_y\rangle = 0$ and $\partial\langle\omega_y\rangle/\partial x < 0$. Note that $\langle\omega_y\rangle = 0$ is equivalent to vanishing shear stress at the bed. Although the present flows are not exactly two-dimensional because of the turbulent bores, we still anticipate that the flow near the bed remains approximately two-dimensional.

[28] Vorticity generation at the bed has a simple relation to the pressure gradient for boundary layer flows [*Lighthill*, 1963]. Because of the no-slip boundary condition (i.e., vanishing inertial force at the boundary), the phase-averaged momentum equation on a plane surface can be reduced to

$$\mu\left(\frac{\partial^2\langle u\rangle}{\partial z^2}\right) = \mu\frac{\partial\langle\omega_y\rangle}{\partial z} = \frac{\partial\langle P\rangle}{\partial x}, \tag{4}$$

where μ is the dynamic viscosity and $\langle P\rangle$ is the excess pressure ($=P + \rho gz$) at the bed surface. Equation (4) means that the flux of vorticity from the bed is created by the pressure gradient. Figure 8 depicts the schematic sketch of vorticity during flow separation at the bore front. Equation (4) indicates that when the pressure gradient in the x direction is negative, the vorticity gradient in the z direction $\partial\langle\omega_y\rangle/\partial z$ is also negative, which means that the positive (CW) vorticity is generated at the bed during the bore front phase. The

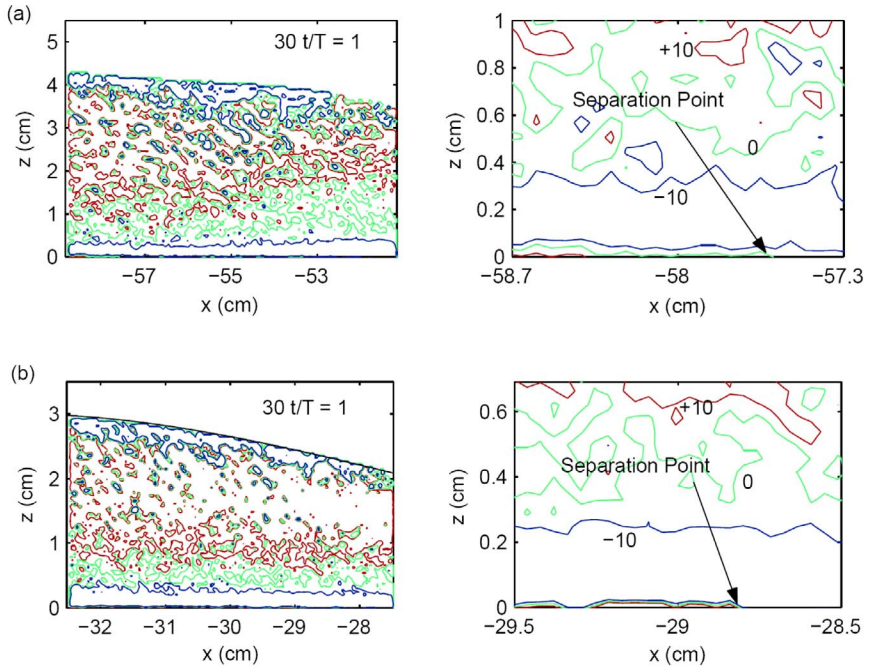

Figure 9. Phase-averaged vorticity contours (s^{-1}) at the phase 30 t/T = 1: (a) $\mathcal{A}_1$ and (b) $\mathcal{A}_2$; red line is $^{-1}0$ s^{-1}, green line is 0 s^{-1}, and blue line is + 10 s^{-1}. The (left) near-bed portion is also shown (right) magnified.

positive vorticity injection below the bed indicated in Figure 8a refers to the flux of vorticity out of the bed due to the negative pressure gradient in the x direction.

[29] In order to satisfy the flow separation condition $\langle\omega_y\rangle$ = 0, there must be a direction change in the vorticity $\langle\omega_y\rangle$ before and after the separation point as indicated in the schematic sketch Figure 8a. The location of the separation point can be identified by plotting the phase-averaged vorticity contours. Figure 9 shows the vorticity contours at the bore front phase 30 t/T = 1 at the measurement locations $\mathcal{A}_1$ and $\mathcal{A}_2$. Our measurements allow us to look closely at the vorticity field $\langle\omega_y\rangle$. The red line, green line, and blue line are the contour lines $\langle\omega_y\rangle$ = + 10, 0, and −10 s^{-1}, respectively. A layer of negative (CCW = blue) vorticity is apparent near the bed in Figure 9 (left), which is advected with the downwash flow. The separation point for Figures 9a (left) and 9b (left) is magnified and shown in Figures 9a (right) and 9b (right). As the bore front passes through the measurement area, the CW vorticity is being generated on the bed as illustrated in Figure 8a. The CW vorticity production due to the negative pressure gradient associated with the bore front interacts with the CCW vorticity originated from the downwash flow, reducing the strength of the CCW vorticity near the bed. Vorticity becomes zero $\langle\omega_y\rangle$ = 0 at some point on the bed, where the flow separation occurs on the bed as shown in Figure 9 for the measurement area $\mathcal{A}_1$ and $\mathcal{A}_2$. We emphasize that the preexisting downwash flow is essential for triggering flow separation. For the measurement area $\mathcal{A}_3$, the separation point cannot be seen from the vorticity contour as the CCW vorticity changes to CW vorticity completely in less than our resolution of phase ($t < t/T$ = 1/30), suggesting that the measurement area at $\mathcal{A}_3$ is sufficiently small that the temporal resolution is insufficient to capture the separation point in a smaller spatial domain at the location $\mathcal{A}_3$ than that at $\mathcal{A}_1$ or $\mathcal{A}_2$. The mechanism to induced flow separation indicate that the separation point advances with the bore front in the onshore direction.

3.4. Flow Reversal

[30] Recall from Figures 3a, 3e, and 3i that in the outer surf zone ($\mathcal{A}_1$), the velocities in the upper water column and near the bed reverse direction almost at the same time, while the velocity at the middepth changes direction later. The near-bed velocity in the boundary layer always responds to the excess pressure gradient earlier than the mid water column velocity, having large inertia, for all the measurement locations. It is remarkable to note that the near-water-surface velocity is also sensitive to the gradient of water surface elevation. At the surface, there is no pressure force (except the air pressure) and it is controlled by the body force. Hence the inertial effect at the surface is quickly responded by the water surface slope, whereas the interior flow must be influenced by the pressure and viscous forces. Figure 10 shows a snap shot of the velocity field at $\mathcal{A}_3$ at the reversal moment (30 t/T = 10). The pressure-driven reversal flow near the bed and the inertial dominant runup flow in the interior result in the formation of a vortex as detected with the streamlines in Figure 10a. As shown in Figure 10b, this vortex is very close to irrotational. It is because the vortex must have been formed by the pressure force, but not caused by viscous diffusion from the boundary. This vortex pattern disappears immediately in the following phase, which is indeed the behavior of a pressure-driven irrotational vortex.

[31] When the flow direction reverses from uprush to downwash, the excess pressure gradient is positive, i.e., the excess pressure is higher at the onshore location relative to

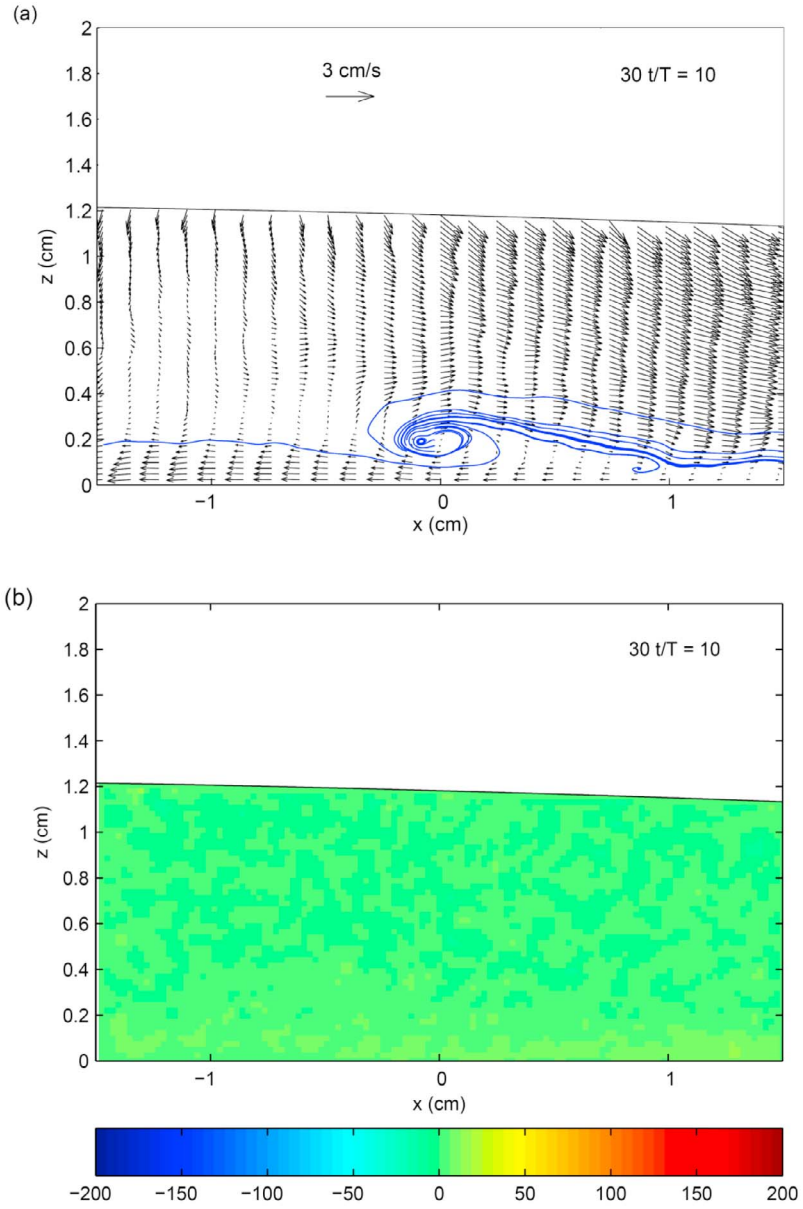

Figure 10. Vortex generation at $\mathcal{A}_3$ during the reversal phase: (a) streamlines (blue) and velocity vector field and (b) vorticity field indicating that the flow is essentially irrotational despite the formation of the clear vortex.

the offshore location. According to equation (4) the negative (CCW) vorticity is generated at the bed boundary along the uprush boundary layer: the uprush boundary layer contains vorticity that is positive (CW). Hence at some point in the reversal process, $\langle \omega_y \rangle$ vanishes, and streamlines intersect at the bed boundary. However, unlike flow separation, $\partial \langle \omega_y \rangle / \partial x$ must be positive. This indicates flow attachment instead of flow separation for two-dimensional flows as shown in the sketch in Figure 8b. Such an attachment flow pattern can be observed near $x = 1$ cm at $\mathcal{A}_3$ in Figure 10a.

3.5. The Velocity Characteristics in the Surf and Swash Zones

[32] The profile of the horizontal velocity component over depth in a wave cycle can be divided into three characteristic intervals. The first interval is the accelerating phases (Figure 11, 30 t/T = 29, 0, and 1). In the surf zone the horizontal velocity near the bed is still directed offshore (Figure 11a). The profile at 30 $t/T = 2$ in Figure 11a is the phase at which the velocity gradient $\partial \langle u \rangle / \partial z = 0$ at the bed, where the flow separation point is located. The CCW (negative) vorticity at the free surface emerges as the water depth increases: this negative vorticity was resulted from the collision of the downwash and uprush flows as we discussed in section 3.2.

[33] The second interval is the stage at which the uprush flow decelerates due to the gravity force (Figure 11, 30 t/T = 2 to 9). It is evident in Figure 11 that the CCW vortex ($\partial \langle u \rangle / \partial z < 0$) at the water surface at $\mathcal{A}_4$ is sustained longer than at $\mathcal{A}_3$. This is partly because the flow depth at

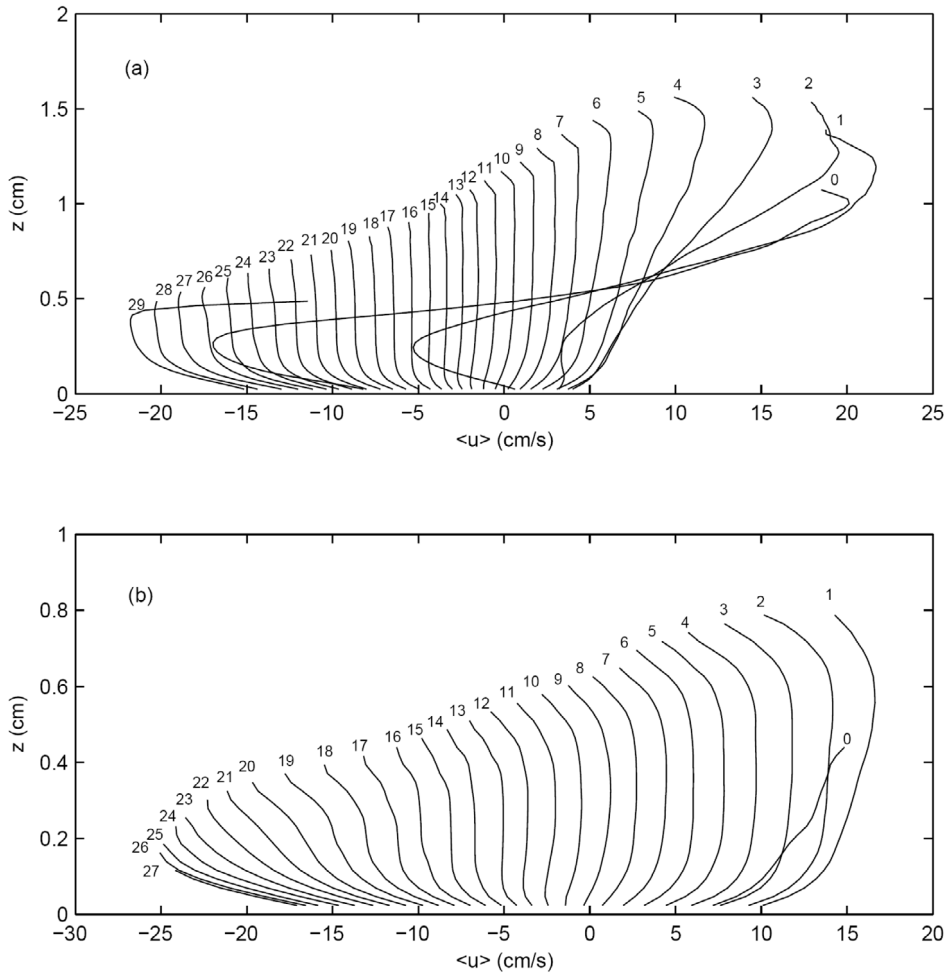

Figure 11. Phase-dependent vertical profile of horizontal velocity averaged across FOV: (a) $\mathcal{A}_3$ and (b) $\mathcal{A}_4$. The numbers represent the phases (= $30t/T$).

$\mathcal{A}_4$ is much shallower and turbulence is weaker relative to $\mathcal{A}_3$; i.e., the momentum mixing of the generated vorticity should be less at $\mathcal{A}_4$ than at $\mathcal{A}_3$. The velocities nearest the bed and the water surface change to the offshore direction first, which implies the fluid near the bottom and the water surface respond to the pressure gradient earlier than the interior fluid. This results in the vortex formation (circulation) when the flow reverses direction, indicating that flow circulation exists in a wave cycle of the flow, although its formation is evanescent and quickly wiped out in the subsequent reversal flow formation. As discussed earlier, this behavior is consistent with that of the irrotational vortex. In spite of the very large ratio of the horizontal wavelength scale to the flow depth in the swash zone, it is not a simple oscillating flow such as the traditional unsteady oscillating boundary layer flow.

[34] The last interval is the phases of downwash accelerating flow driven by gravity (Figure 11, 30 t/T = 10 to 29). In the surf zone (Figure 11a, 30 t/T = 15 to 28), the downwash flow has the characteristics of (negatively) accelerating (consequently thin) boundary layer flows. In the swash zone (Figure 11b, 30 t/T = 17 to 27), the decreasing water depth during the latter part of the downwash eventually causes the boundary layer to saturate the entire flow depth.

[35] Comparing the maximum velocity between the uprush and downwash, the magnitude of the uprush and downwash velocities are very close (22 cm/s) in the surf zone (Figure 11a, 30 t/T = 1 and 29). However, the downwash velocity is 1.66 times the uprush velocity in the swash zone (Figure 11b, 30 t/T = 1 and 26). In spite of the very shallow flow in the swash, the vertical velocity profiles in the most of the uprush and downwash processes are far from uniform for this boundary dominated flow, whereas the uniform velocity profile over the depth is one of the requirements for the shallow-water-wave approximation. The flow speed retardation on the free surface during the uprush process is remarkable for this transient flow. Note that for steady and uniform open channel flows, the maximum velocity is known to be located at some depth below the free surface. The similar but more enhanced velocity profiles are observed in the swash zone (30 t/T = 1 to 10) as shown in Figure 11b.

4. Conclusions

[36] Based on the laboratory experiments using PIV, the following flow characteristics and behaviors in the surf and

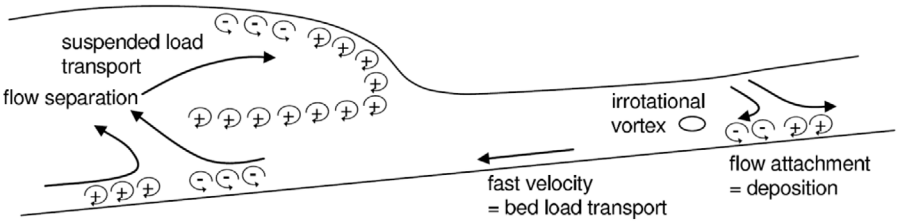

Figure 12. Schematic sketch of the flow structure in the surf and swash zones.

swash zones were found. A summary sketch is shown in Figure 12.

[37] 1. The primary characteristics of the surf zone that differs from the swash zone is the occurrence of flow separation at the bed when the uprush bore meets with the downwash phase. As discussed in section 3.3, flow separation is induced by the large and negative pressure gradient (pointing offshore) caused by the sudden increase in water depth at the bore front. The separation point advances with the bore.

[38] 2. Flow attachment is observed during the flow reversal. A vortex formation was observed near the bed as the flow near the bed responds to the pressure gradient earlier than that in the water column where the inertia effect is significant. This vortex appears to be irrotational and quickly disappears when the flow becomes fully unidirectional.

[39] 3. In the surf zone the thin layer of CCW vorticity on top of the CW vorticity is generated along the water surface due to strong induction of the CW vorticity by the collision of the uprush and downwash flows. We demonstrated that the presence of CCW vorticity on the surface is necessary based on the Stokes theorem. The surface flow pattern can support the presence of CCW vorticity on the surface behind the surface roller.

[40] 4. In the surf zone, the maximum intensity of vorticity occurs at the shear layer in the inner surf zone at the location $\mathcal{A}_3$. The vorticity intensity at the shear layer decreases in magnitude in the offshore locations, indicating that the initial shoreline location $\mathcal{A}_3$ is influenced the most by the vortical flows.

[41] 5. The magnitude of the downwash velocity in the swash zone is greater than that of the uprush process. Therefore, the swash zone flow observed in the experiments should be erosive in the lower part of the swash and accretive in the upper part where flow attachment occurs. The observed velocity profiles over depth in the swash zone deviates substantially from uniform, exhibiting complex vertical structures in such shallow water flows.

[42] 6. Since flow separation occurs at the bore front, the detached sediments from the bed by flow separation must remain suspended by the wave-breaking-generated turbulence and the shear-layer-generated turbulence in the first temporal turbulence interval discussed by *Sou et al.* [2010]. The flow separation underneath the bore front must play an important role in sediment influx as suspended load. Flow attachment occurs at the flow reversal, which is within the second turbulence interval. Since there is no significant mean shear in the water column at the flow reversal, turbulence production is close to zero and the turbulence evolves as free turbulence decay without boundaries [*Sou et al.*, 2010]. The suspended sediments should deposit on the bed with the flow attachment process as the wave-breaking-generated turbulence and the shear-layer-generated turbulence levels become relatively low at the flow reversal.

[43] **Acknowledgments.** This study was supported by the National Science Foundation (grants OCE-0095834, CMS-0245206, and CMS-0324498), the Office of Naval Research (grants N00014-99-1-0193 and N00014-99-1-0591), the Oregon Sea Grant Program (grants NA06OAR4170010-NB154L and NA10OAR4170059-NA223L), and the Oregon State University Edwards Endowment. I. M. Sou is grateful to Edwin A. Cowen and Philip L.-F. Liu for the experimental measurements.

References

Battjes, J. A. (1974), Surf similarity, paper presented 14th International Conference on Coastal Engineering, Am. Soc. of Civ. Eng., Copenhagen.

Butt, T., P. Russell, J. Puleo, J. Miles, and G. Masselink (2004), The influence of bore turbulence on sediment transport in the swash and inner surf zones, *Cont. Shelf Res.*, *24*, 757–771.

Chang, K.-A., and P. L.-F. Liu (1996), Measurement of breaking waves using particle image velocimetry, paper presented at 25th International Conference on Coastal Engineering, Am. Soc. of Civ. Eng., Orlando, Fla.

Chang, K.-A., and P. L.-F. Liu (1998), Velocity, acceleration and vorticity under a breaking wave, *Phys. Fluids*, *10*, 327–329.

Chang, K.-A., and P. L.-F. Liu (1999), Experimental investigation of turbulence generated by breaking waves in water of intermediate depth, *Phys. Fluids*, *11*, 3390–3400.

Cowen, E. A., I. M. Sou, P. L.-F. Liu, and B. Raubenheimer (2003), Particle image velocimetry measurements within a laboratory generated swash zone, *J. Eng. Mech.*, *129*, 1119–1129.

Cox, D. T., and S. L. Anderson (2001), Statistics of intermittent surf zone turbulence and observations of large eddies using PIV, *Coastal Eng. J.*, *43*, 121–131.

Dabiri, D., and M. Gharib (1997), Experimental investigation of the vorticity generation within a spilling water wave, *J. Fluid Mech.*, *330*, 113–139.

Feng, T., and P. K. Stansby (2005), Streamline topography in periodic surf zone waves from LDA measurements, *Meas. Sci. Technol.*, *16*, 1929–1936.

Holland, K. T., B. Raubenheimer, R. T. Guza, and R. A. Holman (1995), Runup kinematics on a natural beach, *J. Geophys. Res.*, *100*, 4985–4993.

Hughes, S. A. (2004), Estimation of wave run-up smooth, impermeable slopes using the wave momentum flux parameter, *Coastal Eng.*, *51*, 1085–1104.

Hwung, H. H., K. S. Hwang, W. S. Chiang, and C. F. Lai (1998), Flow structures in swash zone, paper presented at 26th International Conference on Coastal Engineering, Am. Soc. of Civ. Eng., Reston, Va.

Lighthill, M. J. (1963), Introduction: Boundary layer theory, in *Laminar Boundary Layers*, edited by L. Rosenhead, pp. 46–113, Oxford Univ. Press, Oxford, U. K.

Melville, W. K., F. Veron, and C. J. White (2002), The velocity field under breaking waves: Coherent structures and turbulence, *J. Fluid Mech.*, *454*, 203–233.

Nadaoka, K., and T. Kondoh (1982), Laboratory measurements of velocity field structure in the surf zone by LDV, *Coastal Eng. Jpn. 25*, 125–145.

Petti, M., and S. Longo (2001), Turbulence experiments in the swash zone, *Coastal Eng.*, *43*, 1–24.

Raubenheimer, B. (2002), Observations and predictions of fluid velocities in the surf and swash zones, *J. Geophys. Res.*, *107*(C11), 3190, doi:10.1029/2001JC001264.

Raubenheimer, B., and R. T. Guza (1996), Observations and predictions of run-up, *J. Geophys. Res.*, *101*, 25,575–25,587.

Raubenheimer, B., S. Elgar, and R. T. Guza (2004), Observations of swash zone velocities: A note on friction coefficients, *J. Geophys. Res.*, *109*, C01027, doi:10.1029/2003JC001877.

Sou, I. M., E. A. Cowen, and P. L.-F. Liu (2010), Evolution of the turbulence structure in the surf and swash zones, *J. Fluid Mech.*, *644*, 193–216.

Stive, M. J. F. (1980), Velocity and pressure field of spilling breaker, paper presented at 17th International Conference of Coastal Engineering, Am. Soc. of Civ. Eng., Sydney, N. S. W., Australia.

Ting, F. C. K., and J. T. Kirby (1994), Observation of undertow and turbulence in a laboratory surf zone, *Coastal Eng.*, *24*, 51–80.

Ting, F. C. K., and J. T. Kirby (1995), Dynamics of surf-zone turbulence in a strong plunging breaker, *Coastal Eng.*, *24*, 177–204.

Ting, F. C. K., and J. T. Kirby (1996), Dynamics of surf-zone turbulence in a spilling breaker, *Coastal Eng.*, *27*, 131–160.

Yeh, H. H. (1991), Vorticity-generation mechanisms in bores, *Proc. R. Soc. A*, *432*, 215–231.

Yeh, H. H., A. Ghazali, and I. Marton (1989), Experimental study of bore run-up, *J. Fluid Mech.*, *206*, 563–578.

I. M. Sou, Department of Civil and Environmental Engineering, University of Hawai'i at Mānoa, 2540 Dole St., Holmes Hall 383, Honolulu, HI 96822, USA. (isou@hawaii.edu)

H. Yeh, School of Civil and Construction Engineering, Oregon State University, 201 Graf Hall, Corvallis, OR 97331, USA.